# Evaluation of Ultrasonic Battery Inspection Techniques

Webster, M.*[a], Juarez, P., Frankforter, E.[a]

[a]NASA Langley Research Center, 3 E. Taylor St., Hampton, VA, USA 23681

## ABSTRACT

Lithium metal batteries are prone to subtle defects such as internal dendrites, which can cause internal short circuits and lead to catastrophic ignition. These defects are often undetectable by battery management systems, prompting the need to advance the development of nondestructive evaluation (NDE) techniques for battery applications. Ultrasonic inspection techniques are being evaluated as a means of identifying flaws and irregular lithium plating that can be a precursor to dendrite formation and, ultimately, battery failure.

Two ultrasonic approaches were compared in this study to assess their relative merits for battery inspection. The first was local ultrasonic resonance spectroscopy (LURS), which measures the local through-thickness resonances of the battery to detect changes in structure. The second technique was guided wave ultrasound, which was assessed for its potential for in situ monitoring. Guided wave testing was performed via pitch-catch testing using piezoelectric electric wafer active sensors (PWAS), as well as line scans via laser Doppler vibrometry (LDV). Both measurement modes were applied to lithium metal pouch cell batteries seeded with lithium chips emulating localized plating. The results show the ability to detect and monitor the internal structure of batteries for relatively coarse defects and highlight use cases for each of the two inspection modalities.

**Keywords:** Ultrasound, lithium metal batteries, guided waves, nondestructive evaluation

## INTRODUCTION

Increased demand for portable electric power in recent years has driven a need for high energy density batteries. Lithium metal anodes in rechargeable batteries enable significant energy density improvements over commercially available lithium-ion chemistries. However, there are risks associated with lithium metal batteries that limit their adoption. These risks include thermal runaway and spontaneous ignition of battery cells. One known cause of thermal runaway is non-uniform lithium plating leading to formation of needle-like dendrites. Once formed, dendrites can continue growing during charge/discharge cycles until penetrating the anode/cathode separator and short circuiting the cell [1]. Safe operation of high energy density batteries in aerospace and transportation applications requires the ability to identify precursors to catastrophic failure so that batteries can be removed before they are unsafe. Nondestructive evaluation (NDE) approaches are being developed with this goal in mind.

Ultrasonic NDE techniques are sensitive to changes in the internal structure and mechanical properties of batteries. This sensitivity has been used to assess the performance characteristics and damage state of batteries. Hsieh et al. used ultrasound to track the state of charge by looking at how elastic properties change as ions are transported during charge cycles [2]. Ladpli et al. applied guided wave inspections using externally mounted piezoelectric sensors to detect state of charge (SOC) and state of health (SOH) [3], [4]. Methods in which resonance frequencies are measured to gain information about the structure have also been developed. Rus et al. [5] demonstrated a local ultrasonic resonance spectroscopy (LURS) technique for immersion scan plate inspection. Nelson later applied a

contact transducer variant of LURS to lithium metal pouch cell batteries and developed an accompanying poroelastic model that showed good agreement with experimental results for seeded lithium metal defects [6]. Huang et al. looked at resonance in multi-layer lithium-ion batteries and used that information to visualize the internal stacking sequence of the battery [7]. Gold et al. used time domain and frequency domain measurements on stacked battery materials to extract mechanical properties including wave speeds and acoustic impedances [8].

In this work, two techniques are evaluated for measuring the internal structure of lithium metal batteries. The first is the LURS technique used by Nelson [6], but applied in a scanning form-factor to spatially resolve differences in resonance across the electrode surface. The second is guided wave ultrasound excited by piezoelectric wafer active sensors (PWAS). Surface displacement profiles collected using a laser Doppler vibrometer (LDV) are used to identify fundamental guided wave modes in the battery cells. In addition, PWAS pitch-catch measurements suitable to in situ inspection are performed. Techniques are evaluated on lithium metal pouch cell batteries seeded with internal lithium defects of different sizes on the anode surface. The performance of each technique is shown and use cases for each are discussed.

# TECHNICAL BACKGROUND

## 1.1 Local Ultrasonic Resonance Spectroscopy

The Local Ultrasonic Resonance Spectroscopy approach evaluates through-thickness vibrational resonances of a material locally using a conventional damped piezoelectric transducer. At the material's resonance frequency, acoustic energy is transmitted more easily into the material than away from resonance, resulting in a minimum in the reflection coefficient. Examining the reflection spectrum over a range of frequencies produces a unique "fingerprint" of the material's acoustic response. This response is affected by the internal structure and elastic properties, thus allowing changes in structure associated with damage development in batteries to be identified.



Figure 1: Illustration of LURS testing concept

For a simple case of an LURS measurement of a single layer material enclosed by infinite domains on either side (Error: Reference source not found), the reflection coefficient is given by the expression [6]

$$R = \frac{P1_R}{P1_i} = \frac{\left(1 - \frac{Z_1}{Z_3}\right)\cos\left(k_2 L\right) + i\left(\frac{Z_2}{Z_3} - \frac{Z_1}{Z_2}\right)\sin\left(k_2 L\right)}{\left(1 + \frac{Z_1}{Z_3}\right)\cos\left(k_2 L\right) + i\left(\frac{Z_2}{Z_3} + \frac{Z_1}{Z_2}\right)\sin\left(k_2 L\right)} . \tag{1}$$

$P1_R$ and $P1_i$ are the reflected and incident pressure fields, respectively, $Z_j$ ($j$ = 1,2,3) is the acoustic impedance of layer $j$, and $k_2$ and $L$ are the wavenumber and thickness of the material under test. The wave number is defined as $k_2 = \omega / c_2$ where $\omega$ is the angular frequency of the incoming acoustic wave and $c_2$ is the wave speed of the material under test. The reflection spectrum (i.e., the frequency dependence of the reflection coefficient) is a result of the
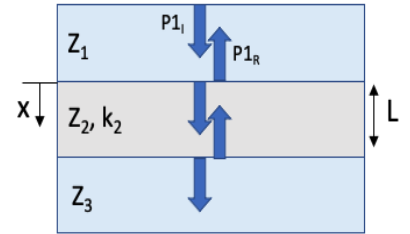
frequency dependence of the wave number $k_2$. For a single layer, the local resonance is driven by the thickness and stiffness (and thus wave speed) of the test article. However, for a layered structure like a pouch cell battery, the resonance of various layers leads to a more complex spectrum that can be used to identify changes in the internal structure related to damage or aging.

For inspection of thin materials (e.g., pouch cell batteries) a delay line is needed to separate the transducer excitation from the measurement signal. The influence of the delay line and instrumentation on the reflection spectrum can be removed by leveraging the linearity of the measurement system [6]. For a linear pulse echo measurement system consisting of electronics, a transducer, a delay line, and an object under test, the voltage applied to the transducer during excitation can be related to the voltage received by the transducer, including a full ringdown of all transmissions and reflections through the specimen, via

$$\left(V_{out}\right)_{meas} = V_\cdot \times H_{el} \times H_{tr} \times H_{FF} \times H^*_{NF} \times H_R \times H^*_{NF} \times H_{FF} \times H_{tr} \times H_{el}, \tag{2}$$

where $H_{el}$ and $H_{tr}$ are transfer functions for the electronics and transducer, the delay line transfer function is broken into far-field ($H_{FF}$) and near-field ($H_{NF}*$) components, and $H_R$ is the transfer function for the material under test. For a reference measurement made without a specimen in the acoustic path, the output voltage is given by

$$\left(V_{out}\right)_{cal} = V_\cdot \times H_{el} \times H_{tr} \times H_{FF} \times H'_{NF} \times H'_{NF} \times H_{FF} \times H_{tr} \times H_{el}. \tag{3}$$

Note that in this case the near field transfer function for the delay line is denoted by $H_{NF}'$ and this is different than the near field transfer function when in contact with the battery surface. The battery's response can be decoupled from the instrument and delay line by dividing Equation (2) by Equation (1):

$$\left|R(\omega)\right| = \frac{\left|\left(V_{out}\right)_{Meas}\right|}{\lnot\left(V_{out}\right)_{cal} \vee \lnot = \lnot H_{NF} \vee \times \vee H_R\left|\times\lnot H_{NF}\right|\lnot}, \tag{4}$$

where in this case the near field effects from the measurement and calibration steps have been combined into a single term, $H_{NF} = H_{NF}*/H_{NF}'$. This near field term will play a role in the observed amplitude of the reflection coefficient, but not in its resonance frequencies [6]. In this study the primary metrics of interest for assessing battery structure are the frequencies at which resonances occur in the reflection coefficient defined in Equation (4).

## 1.2 Guided Wave Ultrasound

Guided wave ultrasound involves the propagation of waves along boundaries or discontinuities. The classical Lamb wave analysis for guided wave propagation in isotropic plates [9] may be used as a qualitative foundation for the more complex problem of combined elastic and porous 'plate-like' geometry assessed in this study. The guided waves propagate in multiple modes, with the velocity and number of modes dictated via the excitation frequency and dispersion curve for the media and geometry. See Figure 1 for an exemplary group velocity dispersion curve for a Lamb wave in isotropic media. The wave modes have a

thickness-mode resonance that couples through the entire thickness, with lateral propagation according to the specimen's dispersion curve. This lateral propagation allows for large area coverage, which makes guided wave analysis a strong technique for ultrasonic NDE and structural health monitoring (SHM) methodologies.
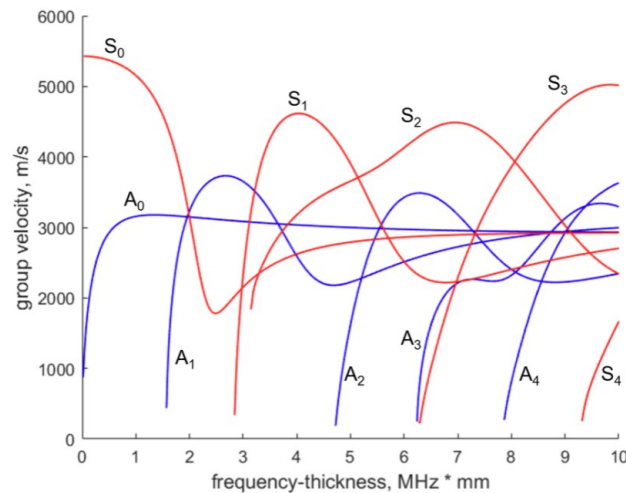


*Figure 1: Exemplary group velocity dispersion curve for Lamb wave in aluminum 2024. Red lines indicate symmetric wave modes, and blue lines indicate antisymmetric wave modes.*

Various guided wave formulations are available for varying conditions such as layered transversely isotropic composites [9] and anisotropic up to triclinic media [10]. Notably, for porous media such as battery separator materials and the cathode in lithium metal batteries, the equations of motion are treated via Biot poroelasticity (in the isotropic case) [11]. Gilbert et al. [12] has produced a Lamb wave formulation for poroelastic media; however, it is limited to a single layer, where pouch cells may contain many dozens of individual layers. Thus, previous battery guided wave studies have relied on isotropic Lamb wave formulations, deliberately omitting effects such as a second slow pressure wave existent in the porous components [4]. In this study, rather than attempt to generalize a Lamb wave formulation in a quantitative manner, which would be beyond the scope of the current investigation, empirical observations are drawn related to general guided wave principles.

## METHODS

### 1.3 Specimen Development

Lithium metal pouch cell batteries were made for this study by Cornerstone Research Group. The batteries consisted of a nylon/aluminum/polypropylene pouch, lithium metal anodes on a copper current collector, lithium cobalt oxide ($LiCoO_2$) cathodes on an aluminum current collector, and Celgard[i] 2325 separators between the anode and cathode layers. The liquid electrolyte consisted of $LiPF_6$ dissolved into a solution of equal parts ethylene carbonate, dimethyl carbonate, and diethyl carbonate.

To emulate the type of localized plating that could lead to dendrite growth and short circuiting, chips of 80$\mu$m-thick lithium metal were pressed onto the anode surface during fabrication in select locations. One defective specimen and one pristine baseline specimen were produced. Lithium chip sizes used in this study ranged from 3mm to 16mm in diameter and had an arrangement shown below in Figure 2.
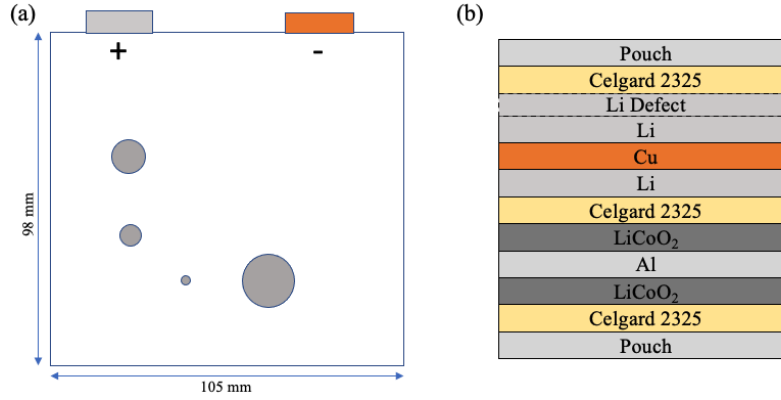
*Figure 2: Illustration of the lithium metal pouch cell seeded with 80μm-thick lithium defects. (a) spatial distribution and relative sizes of defects. (b) Through-thickness stacking sequence of the pouch cell.*

## 1.4 Local Ultrasonic Resonance Spectroscopy

LURS measurements were made using a 5MHz contact ultrasonic transducer with an acrylic delay line which was excited by an Olympus[i] 5073PR pulser-receiver. The transducer was mounted to a computer-controlled scanning gantry programed to perform contact measurements across a 2.8" x 1.8" area on the battery surface. Measurements were made at 0.05" increments in the x- and y-directions. At each measurement point the z-axis was moved into contact with the specimen surface with a pressure of roughly 16psi and data was recorded through an oscilloscope. After each battery inspection, baseline data was collected without the specimen present (i.e., only the delay line in contact with the transducer).

Time series data were collected at each inspection point and the root mean squared (RMS) amplitude was recorded over a ~1.6μs window positioned at three different time gates: (a) one centered on the main echo received from the battery, (b) one offset by 1.6μs from the start of the first gate, and (c) one offset by 3.2μs from the start of the first gate. The thin nature of the battery made it impossible to distinguish between front wall and back-wall echoes. Amplitude data from each inspection point were compiled into C-scan plots for visualization.

The battery's reflection spectrum was calculated from the time domain data by first centering, zero-padding, and applying a Hanning window to the time data. A fast Fourier transform (FFT) was applied to convert to the frequency-domain and the FFT data was normalized by data collected for just the transducer and delay line to produce the reflection coefficient described by Equation (4). The reflection coefficient was calculated at each inspection location and Matlab®[i] was used to track local minima. As discussed in Section 1.1, these minima in the reflection coefficient occur at the battery's resonance frequencies [6]. The frequency of the first and second resonance, f1 and f2, and the associated widths at half minimum, w1 and w2 (Figure 3) were calculated at each point and compiled into c-scan plots for visualization.
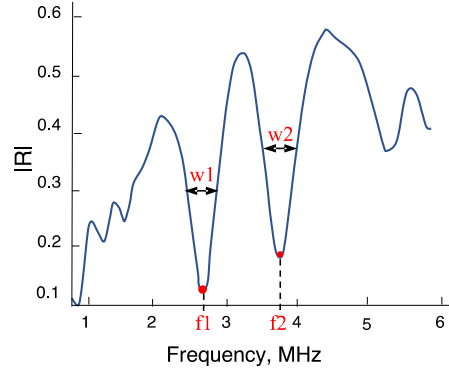
*Figure 3: Reflection coefficient as a function of frequency, with an illustration of the peak tracking parameters that extracted at each inspection point – the first resonance frequency (f1) and width at half min (w1), and the second resonance frequency (f2) and width at half min (w2).*

## 1.5 Guided Wave Inspections

Two methods of guided wave inspection were used in this work: (a) pitch-catch testing using piezoelectric wafer active sensors (PWAS), and (b) laser Doppler vibrometry (LDV) line scans. The pitch-catch testing helps to assess the potential for low cost, practical SHM techniques, and the LDV testing provides further insight into wave propagation characteristics.

The baseline and defective lithium metal pouch cells were instrumented with 7-mm diameter, 0.2-mm thick PWAS comprised of SM412 material (STEMiNC[i] Part No. SMD07T02R412WL). The PWAS were permanently bonded to the battery pouch material, using Micro-Measurements[i] M-Bond 200 cyanoacrylate adhesive. The bonding was performed after the LURS testing was complete. For the baseline specimen, the PWAS were bonded roughly along the centerline of the pouch cell (Figure 4a). For the defective specimen, the PWAS were bonded adjacent to the lithium chips (Figure 4b), allowing the potential to capture scattering from these defects.
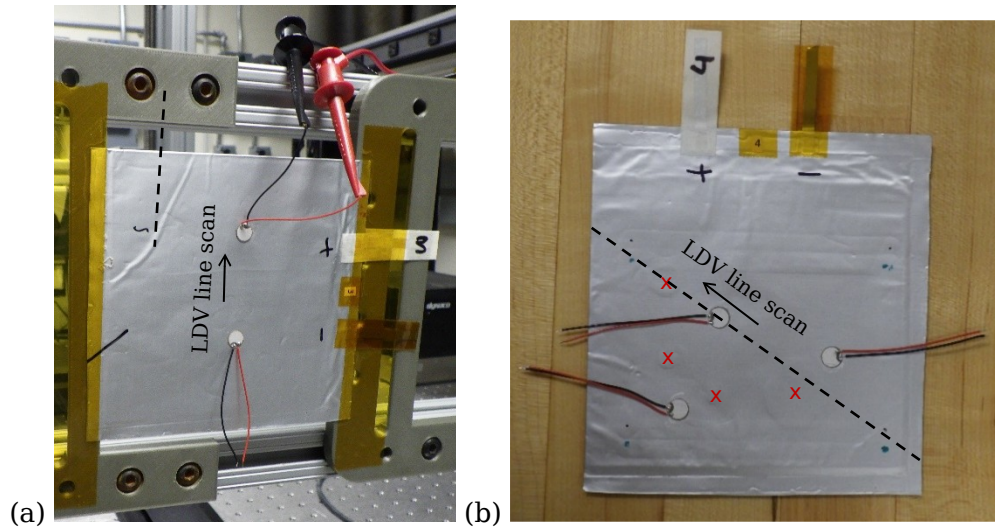


(a)　　　　　　　　(b)

*Figure 4: Lithium metal pouch cell instrumented with PWAS for guided wave testing. (a) pristine pouch cell, and (b) defective pouch cell with four lithium chip locations indicated with red marks. LDV line scans were performed along the dashed lines, with the arrow indicating the direction of the scan.*

For pitch-catch testing, the top PWAS in Figure 4a was used for excitation, and the bottom used as a receiver. For the defective specimen, the top-left PWAS in Figure 4b was used for

excitation, and the right-hand PWAS adjacent to the large lithium chip was used as a receiver. A $20V_{pp}$, 300 kHz 3-count sine wave was used for excitation using a Keysight[i] 33600A waveform generator, and the received signal was averaged 128 times, measured using a Teledyne LeCroy[i] HDO6054 oscilloscope. The resulting waveforms were digitally filtered using a 500 kHz lowpass filter to improve the signal-to-noise ratio and mitigate any electromagnetic interference (since the PWAS are not shielded from electromagnetic interference like conventional ultrasonic transducers).

LDV line scans were performed on each specimen using a Polytec[i] VibroFlex-Xtra VFX-I-120 LDV (Figure 5a). The same excitation PWAS from the pitch-catch measurements were used for the LDV measurements. Scans were performed on the side of the pouch opposite from the PWAS (Figure 5b). A $5V_{pp}$ 100 kHz 5-count Hann windowed sine wave was excited. The LDV output was passed through a NI[i] PXIe 14-bit 100MS/s digitizer and averaged 128 times. The scan was performed in 100 µm increments while maintaining the laser scan head perpendicular to the pouch cells for each scan point. The LDV's received laser signal strength was tracked and re-focused anytime it dropped below 60%.
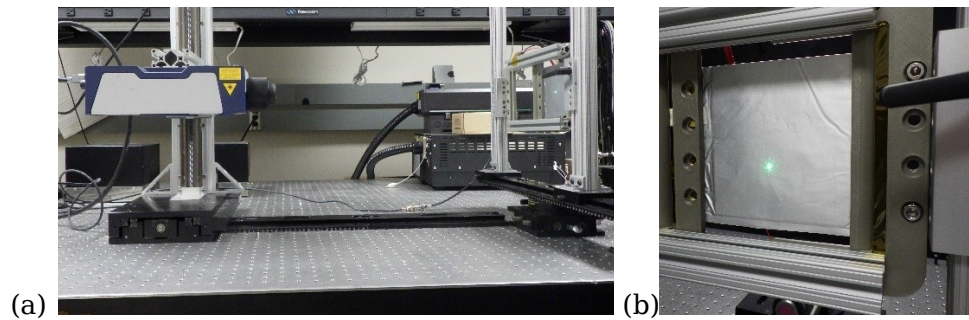

(a)                                        (b)

*Figure 5: (a) LDV line scan in progress, and (b) pouch cell mounted in fixture*

# RESULTS

## 1.6 Local Ultrasonic Resonance Spectroscopy

Time domain data collected during scanning inspections of the defective pouch cell battery is shown in Figure 6. At the top of the figure, three amplitude maps (Figure 6a – Figure 6c) are given, corresponding to the RMS amplitude at each pixel location of three different time gated regions (labeled TG1, TG2, and TG3). Within Figure 6a – Figure 6c, two regions are highlighted by colored circles. These indicate where the time traces shown in Figure 6d were collected. The red circle is over a lithium chip, while the blue region is both free of defects and away from any edge regions. Note that the diameter of the red and blue circles approximate the diameter of the transducer used in the inspection.
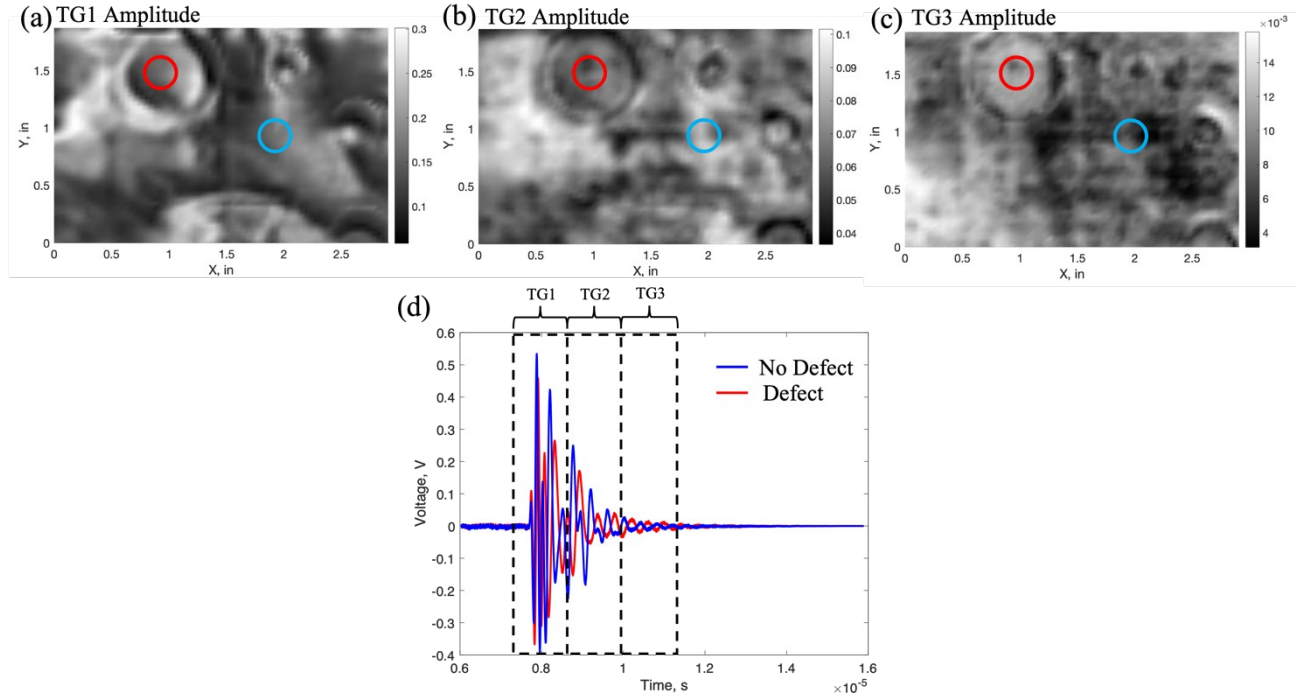
*Figure 6: Time domain data collected on the defective battery specimen. (a) RMS amplitude calculated over time gate 1 (TG1), (b) RMS amplitude calculated over time gate 2 (TG2), (c) RMS amplitude calculated over time gate 3 (TG3), (d) Time traces (A-scans) collected in the regions highlighted in the amplitude map images. Blue – No defect, Red, - Defect.*

The presence of defects in the specimen is clear in each amplitude plot shown in Figure 6a – Figure 6c, but contrast is somewhat improved for later time gates (TG2 and TG3). In the first two time gates the defective region has a lower RMS amplitude than the defect-free region, but it has a higher amplitude in the last gate (TG3).

The time-domain data were processed to calculate the reflection spectrum at each pixel location. In Figure 7, resonant frequency maps for the first resonance (Figure 7a) and second resonance (Figure 7b) show particularly good contrast to defects. The impact of the defects can also be seen in plots of the peak width (Figure 7c and Figure 7d). The width data seems more sensitive to edge effects and also possibly to slight changes in coupling condition. The result is more variation than seen in the frequency data.
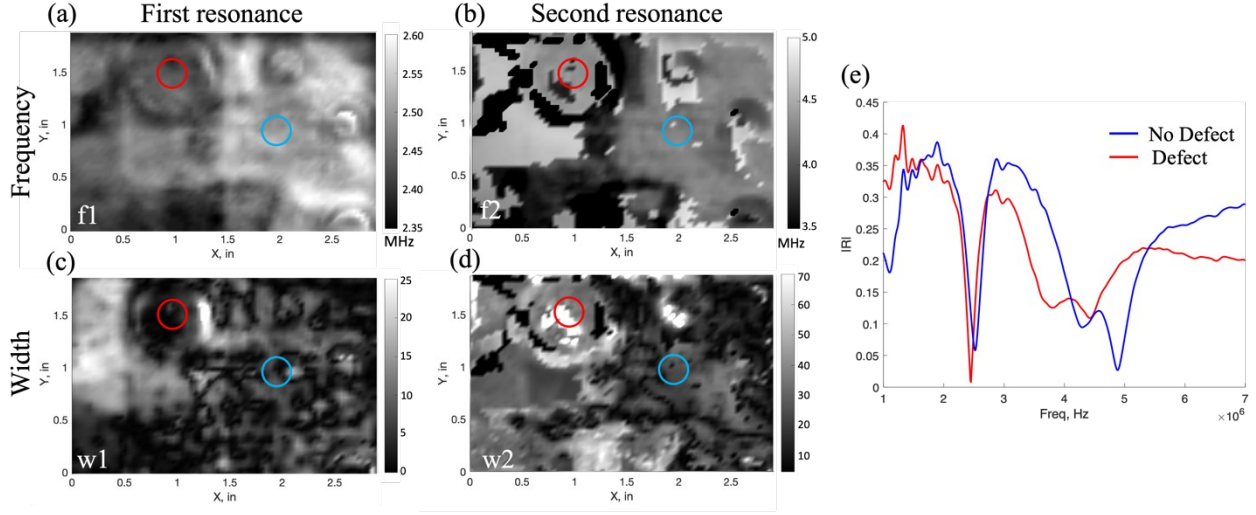
*Figure 7: Reflection coefficient data collected on the defective battery specimen. (a) Frequency of the first resonance peak, f1, (b) Width at half min for the first resonance peak, w1, (c) Frequency of the first resonance peak, f2, (d) Width at half min for the second resonance peak, w2, (e) Reflection spectra for two highlighted regions. Blue – No defect, Red, - Defect.*

The results in Figure 7 show general agreement with those presented by Nelson in [6] in that a shift in the resonance frequencies toward lower frequencies was observed due to the presence of the 16mm lithium chip, with the largest change observed in the second resonance frequency. This is seen in the resonance spectra shown in Figure 7e, which is collected from the regions highlighted by red and blue circles (for defect and non-defect regions, respectively) in Figure 7a-d.

## 1.7 Guided Wave Ultrasound

Pitch-catch waveforms for the baseline and defective pouch cells are shown in Figure 8. The amplitudes were normalized for comparison of guided waves traveling over different propagation distances. Both results had large, visible waveforms indicating strong coupling of energy between the transducers and the pouch cell, and clear signal propagation across the cell. The waveform in the pristine pouch cell (Figure 8a) shows what appears to be one distinct wave packet between 0-50 µs. However, it shows more peaks than would be indicated by the 3-count tone burst excitation. This appears to indicate that the wave packet has split into multiple modes which are either very close in group velocity, or have not propagated over a large enough distance to separate in the time domain. A low-amplitude, low-frequency signal is present after the initial wave packet arrival. The source of this is unclear, but could be due to factors such as edge reflections or electrical noise. Additionally, note that some reflections from the PWAS are possible, but are expected to be a second order effect as PWAS reflections would be visible in both the pristine and defective pitch-catch results if the effects were large.

Assessing the received pitch-catch waveform for the defective specimen in Figure 8b, the same initial large-amplitude waveform is present, with a second smaller wave packet from approximately 50-100 µs. This wave packet is not present in the pristine battery, indicating it is not expected to be due to reflections from lateral edges. Rather, this is consistent with reflection and internal reverberation radiating from the large lithium chip adjacent to the receiver PWAS. This is somewhat analogous to previous descriptions of wave trapping effects in finite-sized delaminations in composite specimens [13]. This evidence demonstrates the feasibility of using guided waves for sensing embedded defects in pouch cells.
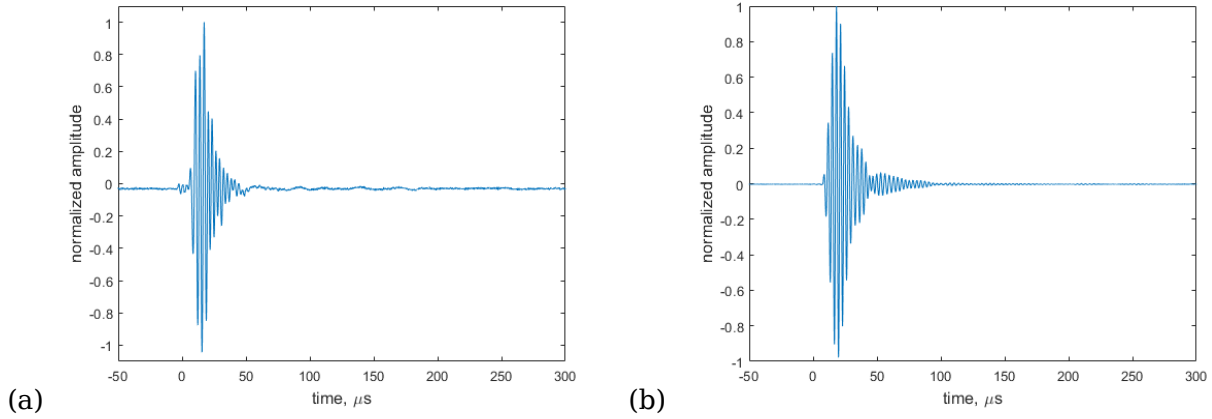
*Figure 8: Pitch-catch results for (a) baseline, and (b) defective pouch cells.*

Space-time B-scans of the baseline and defective LDV results are shown in Figure 9 (with the scan starting at 0 mm and moving in the direction of the arrow previously noted in Figure 4). The colormap of the Figure 9b B-scans were saturated to 10 times lower than the peak value to aid with visualization of modes with lower out-of-plane velocity amplitude. Examining the baseline pouch cell in Figure 9a, two distinct wave modes are present (visible by two different slopes representing each mode's group velocity). A faster propagating, lower amplitude mode is visible, and this appears to be consistent with a fundamental symmetric mode, which travels at faster group velocities at lower frequencies (for reference, see the S0 mode in Figure 1). Additionally, a lower amplitude is expected from the fundamental symmetric mode since its motion is in-plane dominant (and not strongly detected by the LDV which is measuring out-of-plane velocity). The higher amplitude, slower moving mode would then be the fundamental antisymmetric mode. Note that there is almost a complete lack of scattering (with one exception at around 30 mm where the second receiver PWAS was bonded for the pitch-catch tests).

Next, examining the space-time plot of the defective pouch cell in Figure 9b, the same two modes appear to be present (exhibiting the same slope). Interestingly, the same two modes identified in Figure 9a are present; however, a third wave mode is present in Figure 9b, traveling even slower than the antisymmetric mode identified in the baseline specimen. Without a dispersion curve formulation, it is difficult to label this third mode; however, it is present across the length of the scan and thus not associated with the defects. Some of the components, notably the separator, have been reported to be anisotropic [15], and since this scan was rotated to cover two lithium chips, this may be a factor. A second notable feature is rippling in the wave modes as they propagate over aberrations. These aberrations include not only the lithium chips, but also indentations the LURS inspection left on the pouch cell (e.g., the lines visible at the top of Figure 4b).
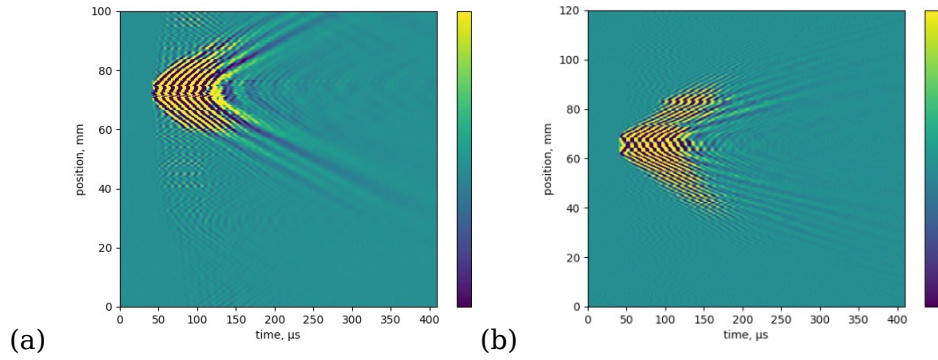
(a)                                                    (b)

*Figure 9: LDV B-scans showing guided wave propagation for (a) baseline pouch cell, and (b) defective pouch cell*

In Figure 10, the out-of-plane velocity waveforms obtained by the LDV are shown for the pristine specimen at 80 and 95 mm, with respect to the position shown in Figure 9. Comparing Figure 9a and Figure 9b, a separation in what is presumed to be fundamental (faster) symmetric and (slower) antisymmetric wave modes is observed. Additionally, a rapid decline in the magnitude of the out-of-plane velocity is observed, indicating a high degree of attenuation. This is a significantly higher degree of attenuation compared to what is typically seen in isotropic elastic media, and may be attributed to losses due to factors such as damping caused by the electrolyte viscosity. This factor is also seen in the LURS data, for example the large bandwidth of resonance frequencies in Figure 7e. A similar effect is seen in the defective specimen in Figure 11, which shows a marked drop in amplitude (and also in signal-to-noise ratio) over a propagation distance of only 10 mm.
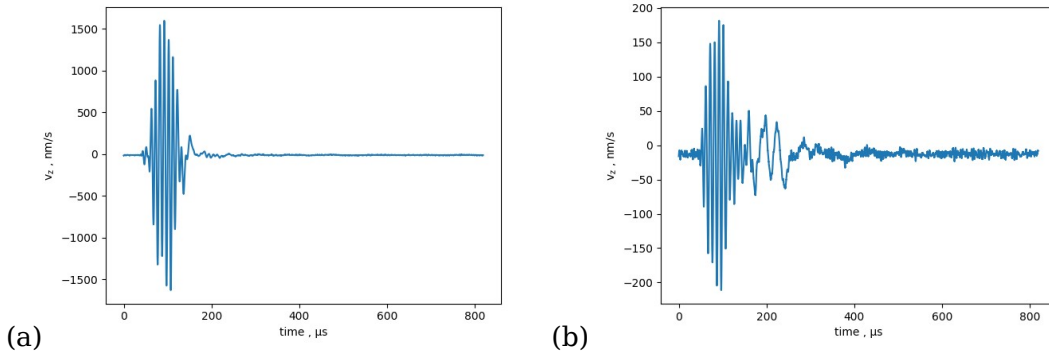


(a)                                                    (b)

*Figure 10: Pristine specimen out-of-plane velocity at (a) 80 mm, and (b) 95 mm. For reference, the PWAS transducer was located at x = 72 mm.*
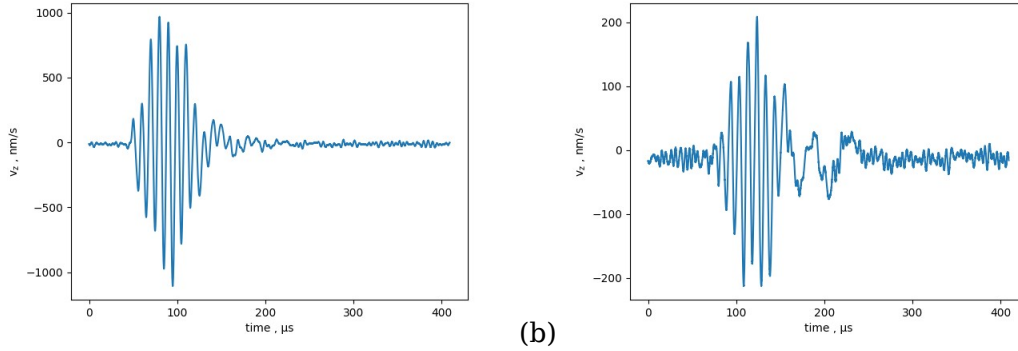
(a)                    (b)

*Figure 11: Defective specimen out-of-plane velocity at (a) x = 60 mm, and (b) x = 50 mm. For reference, the PWAS excitation was located at 65 mm.*

# DISCUSSION

This study evaluated two techniques for inspecting lithium metal batteries. Both techniques were sensitive to localized defects seeded onto the batteries' lithium metal anode but differ in the level of detail provided and their application space. Guided wave inspections have clear potential for in situ monitoring as noted by other researchers (e.g., [3]). On the other hand, pulse echo and LURS inspection of batteries provides a higher level of detail to the internal structure due to the ability to track changes in both the amplitude and resonance frequencies of the battery, but require the specimens to be removed for inspection.

Pulse echo inspection of the battery analyzed in the time domain showed signatures from embedded flaws, but surface irregularities and edge effects dominate the earliest time gates analyzed. As noted in [16], later time gates lead to better resolution of features deep within the layup that continue to reverberate after the main peak of the received signal. The LURS technique improved the contrast to the flaws present in the defective battery and provided information on the structure that underlies variations in amplitude observed in the time domain analysis. The goal in applying this approach in practice would be to apply this knowledge of the resonance peaks in the specimen at a given location to deduce the structure using an inverse modeling approach. For example, using the poroelastic finite element model of a unit cell of the battery described in [6], experimental data obtained regarding local resonance frequencies and peak widths could be used to find a structure and set of poroelastic properties that would yield such resonance behavior through a parametric sweep.

Qualitative analysis of guided wave measurements was successful in identifying defect-associated features, but was unsuccessful in differentiating these features from other contributing factors, such as wrinkling. A second wave packet with a long ringdown was observed in the guided wave pitch-catch measurements. Aberrations associated with lithium chips and wrinkling were observed in the LDV results. It's notable that the pristine region of the dispersion curves differed between tests, possibly due to rotation of the LDV scan line in the presence of anisotropic component materials. It's also notable that the specimen exhibited significant attenuation, consistent with wave propagation through the fluid-filled viscous media. Still, the PWAS pitch-catch results showed a reasonable signal-to-noise ratio and shows promise as a battery SHM modality.

Further guided wave quantitative analysis would benefit from an elastic-poroelastic Lamb wave dispersion curve formulation, either analytical or derived from a numerical model such as finite element modeling (FEM). However, use of such a model would necessitate accurate material properties for solid, fluid, porous, and coupling parameters in the poroelastic media[1]

---

1

(many of which would need to be measured or estimated). Further investigations into methods to accurately measure these properties would yield benefit to both LURS and guided wave models. In the LURS models, accurate material properties and constitutive models would help differentiate between resonance shifts due to elastic property changes, compared to resonance shifts due to flaw conditions. In the guided wave analysis, this would allow accurate predictions of wave propagation behavior, with potential for improved insight and predictions into scattering conditions.

# ACKNOWLEDGEMENTS

# REFERENCES

[1] X. Q. Xu, X. B. Cheng, F. N. Jiang, S. J. Yang, D. Ren, P. Shi, H. Hsu, H. Yuan, J. Q. Huang, M. Ouyang and Q. Zhang, "Dendrite-accelerated thermal runaway mechanisms of lithium metal pouch batteries," *SusMat,* 2022.

[2] A. G. Hsieh, S. Bhadra, B. J. Hertzberg, P. J. Gjeltema, A. Goy, J. W. Fleischer and D. A. Steingart, "Electrochemical-acoustic time of flight: in operando correlation of physical dynammics with battery charge and health," *Energy and Environmental Science,* 2015.

[3] P. Ladpli, F. Kopsaftopoulos and F. Chang, "Estimating state of charge and health of lithium-ion batteries with guided waves using built-in piezoelectric sensors/actuators," *Journal of Power Sources,* 2018.

[4] P. Ladpli, F. Kopsaftopoulos, R. Nardari and F. K. Chang, "Battery charge and health state monitoring via ultrasonic guided-wave-based methods using built-in piezoelectric transducers," *Smart Materials and Nondestructive Evaluation for Energy Systems,* vol. 10171, 2017.

[5] J. Rus and C. Gross, "Local ultrasonic resonance spectroscopy: a demonstration on plate inspection," *Journal of nondestructive evaluation,* 2020.

[6] W. Nelson, "Local Ultrasonic Resonance Spectroscopy of Lithium Metal Batteries for Aerospace Applications," *Master's Thesis, University of Virginia,* 2021.

[7] M. Huang, N. Kirkaldy, Y. Zhao, Y. Patel, F. Cegla and B. Lan, "Quantitative Characterization of the Layered Structure Within Lithium-Ion Batteries using Ultrasonic Resonance," *Journal of Energy Storage,* 2022.

[8] L. Gold, T. Herzog, F. Schubert, H. Heuer and G. Giffin, "Ultrasound Propagation in Lithium-Ion Battery Cell Materials: Basis for Developing Monitoring and Imaging Methods," *Energy Technology,* 2022.

[9] V. Giurgiutiu, Structural Health Monitoring with Piezoelectric Wafer Active Sensors, Academic Press, 2014.

[10] F. H. Quintanilla, Z. Fan and M. Lowe, "Guided waves' dispersion curves in anisotropic viscoelastic single-and multi-layered media," *Proceedings of teh Royal Society A: Mathematical, Physical and Engineering Sciences,* vol. 471, 2015.

[11] M. Biot, "Theory of Propagation of Elastic Waves in a Fluid-Saturated Porous Solid. I. Low-Frequency Range," *Journal of teh Acoustical Society of America,* vol. 28, 1956.

[12] R. P. Gilbert, D. S. Lee and M. Y. Ou, "Lamb waves in a poroelastic plate," *Journal of Computational Acoustics,* 2013.

[13] C. A. Leckey, K. R. Wheeler, V. N. Hafiychuk, H. Hafiychuk and D. A. Timucin, "Simulation of guided-wave ultrasound propagation in composite laminates: Benchmark comparison of numerical codes and experiment," *Ultrasonics,* pp. 187-200, 2018.

[15] S. Kalnaus, Y. Wang and J. Turner, "Mechanical behavior and failure mechanisms of Li-ion

battery separators," *Journal of Power Sources,* vol. 348, 2017.

[i] Specific vendor and manufacturer names are explicitly mentioned only to accurately describe the test hardware.  The use of vendor and manufacturer names does not imply an endorsement by the U.S. Government, nor does it imply that the specified equipment is the best available.